Solar-driven Calcium Looping in Fluidized Beds for Thermochemical Energy Storage

Claudio Tregambi[1,2], Francesca Di Lauro[3], Sara Pascual[4], Pilar Lisbona[4],

Luis M. Romeo[4], Roberto Solimene[2,*], Piero Salatino[5], Fabio Montagnaro[3]

[1] *Dipartimento di Ingegneria, Università degli Studi del Sannio,*

Piazza Roma 21, 82100 Benevento, Italy

[2] *Istituto di Scienze e Tecnologie per l'Energia e la Mobilità Sostenibili,*

Consiglio Nazionale delle Ricerche, Piazzale Tecchio 80, 80125 Napoli (Italy)

[3] *Dipartimento di Scienze Chimiche, Università degli Studi di Napoli Federico II,*

Complesso Universitario di Monte Sant'Angelo, 80126 Napoli, Italy

[4] *Departamento de Ingeniería Mecánica. Escuela de Ingeniería y Arquitectura (EINA).*

Universidad de Zaragoza, C/ María de Luna s/n, 50018, Zaragoza, Spain

[5] *Dipartimento di Ingegneria Chimica, dei Materiali e della Produzione Industriale,*

Università degli Studi di Napoli Federico II, Piazzale Tecchio 80, 80125 Napoli, Italy

*Corresponding Author. E: roberto.solimene@cnr.it (Phone: +390815931567)

Abstract

Integration between Concentrated Solar Power (CSP) and Calcium Looping (CaL) is gaining consideration in the perspective of large shares of renewable energy sources, to smooth the variability of non-dispatchable energy input. The scope of this study is to investigate the CaL process for ThermoChemical Energy Storage (TCES), by performing a dedicated experimental campaign in fluidized bed under realistic process conditions suitable for CaL-CSP integration. Chemical deactivation of the limestone-based sorbent has been assessed by measuring the extent of Ca carbonation along iterated calcination/carbonation cycles, correlated with physico-chemical characterization of the sorbent at selected stages of the conversion. Properties that have been scrutinized were particle size distribution, bulk density and particle size, density, and porosity of bed solids. The attainable values of energy storage density were evaluated as well. A remarkable finding of the experimental campaign is the pronounced synergistic deactivation of limestone when it is co-processed with silica sand. Chemical interaction of CaO with the silica sand constituents at the process temperatures has been scrutinized as possible responsible for the loss of reactive CaO toward CO_2 uptake. Post-process of particle density data, together with N_2-intrusion porosimetric analysis, and quantitative and qualitative XRD analyses, suggests that the sand/lime interaction induces a strong reduction of the total and reactive sorbent porosity and, in turn, of reactivity.

Density-based classification to separate converted and unconverted limestone particles after the carbonation step has been evaluated with the goal of increasing process efficiency, by avoiding the circulation of streams with unreacted particles through the plant. For this purpose, the minimum fluidization velocity of calcined and carbonated particles has been measured after each reaction step at the relevant process temperature.

Keywords

Concentrated solar thermal power; calcium looping; fluidized bed; lime-sand interaction; sorbent deactivation; thermochemical energy storage;

1. Introduction

The ambitious targets of the European Green Deal aim to cut the greenhouse gas emissions by at least 55% within 2030, and to achieve carbon neutrality by 2050 with net-zero greenhouse gas emissions. These objectives require a strong decarbonization of the power and energy sectors, with an ever-increasing exploitation of renewable energy sources. Among them, solar energy is bound to play a key role in the future economy because of its virtual unlimited potential and wide availability. However, a strategy to deal with its intermittent nature needs to be implemented to enable its massive deployment.

Concentrated Solar Power (CSP) technologies provide an effective path for exploitation of solar energy, allowing integration with thermal and thermochemical energy storage systems to overcome its intrinsic intermittency. In CSP systems, a field of heliostats (i.e., sun tracking mirrors) is used to focus and concentrate the solar energy onto a receiver. Here, a heat transfer medium is heated at moderate-to-high temperatures and eventually used to sustain energy intensive chemical/physical processes, or to drive thermodynamic cycles for energy generation. Most recent commercial CSP plants make use of molten salts (i.e., a binary mixture of $NaNO_3$ and KNO_3) as heat transfer medium, which operate within the 290–565 °C temperature range. Storage of the hot medium in insulated vessels, rather than direct use (i.e., thermal energy storage), allows decoupling the two steps of solar energy collection and exploitation, enhancing the dispatchability of solar energy. Research efforts on the CSP technology are mostly prioritized on: i) increasing the maximum working temperature of the heat transfer medium, currently limited at 565 °C due to the molten salts degradation; ii) developing more efficient energy storage systems with respect to storage density, application temperature, and time scale of utilization. On one side, particle receivers are under the spotlight to overcome the temperature limitations of the molten salts: dense-solids suspensions can indeed safely work at temperatures of 1000 °C and over [1–3]. On the other side, use of reversible chemical reactions to store solar energy in the form of chemical bonds (i.e., ThermoChemical Energy Storage, TCES) is widely pursued [4–7]. Gas-solid chemical reactions are the most investigated. Indeed, their higher reaction enthalpy turns into potential higher values of energy storage densities and the easier separation of the reaction products favours the subsequent storage/transportation.

Particle receivers able to simultaneously work as solar receiver and chemical reactor can represent a breakthrough for the success of the CSP-TCES technology. For this reason, Fluidized Bed (FB) systems have been and are widely investigated [8–10]. Literature research studies spread from conventional FB with direct/indirect irradiation [11–13], to innovative design targeted at: i) increasing the axial thermal diffusivity by internal circulation [14–16],

83   spout, pulsed or uneven fluidization [2,17–20]; ii) providing a more uniform residence time

84   distribution by multistage operation [21–23]; iii) exploiting the sensible heat of the reaction

85   products for the heating of the reactants by internal solid-solid heat exchangers [2,24,25].

86   The selection of the most appropriate chemical reaction for TCES is open to debate. Apart from

87   solar fuels production, decomposition and recombination of metal hydroxides, carbonates,

88   oxides and perovskites are among the most investigated processes, each with specific

89   advantages and drawbacks [26–29]. In particular, reversible calcination-carbonation of

90   Ca-based sorbents, Eq. (R_1):

91                        $CaCO_3 \leftrightarrows CaO + CO_2$ (R_1)
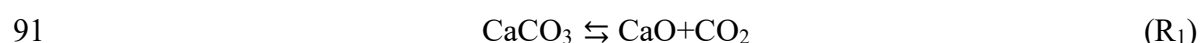
92   has been widely addressed recently, and its integration with CSP is being currently assessed,

93   with different European research projects currently active [30,31].

94   The same reaction scheme has been widely investigated in literature for post combustion and

95   atmospheric CO_2 capture, and is commonly referred to as Calcium Looping (CaL) [32–35].

96   CSP-CaL integrated processes targets both CO_2 capture [34,36,37] and TCES. The interest on

97   this system for TCES applications mainly springs from: i) the fairly high reaction enthalpy of

98   the chemical reaction ($|\Delta H_r°|_{298K}=178$ kJ mol^{-1}); ii) the high temperature at which solar energy

99   can be retrieved (650–850 °C according to the process parameters), which allows integration

100   with high-efficiency Rankine/Brayton cycles [38]; iii) the low cost of the raw material (i.e.,

101   limestone, a very cheap natural sorbent rich in $CaCO_3$). On the other side, the major weakness

102   of the CaL cycle is the decay of material reactivity over iterated cycling, induced by loss of

103   porosity (i.e., thermal/chemical sintering) and pore plugging [39–41]. Different techniques have

104   been explored to prevent or limit the loss of reactivity, among which: production of composite

105   materials with inert stabilizers/promoters [42] such as ZrO_2 [43–45], Al_2O_3 [46,47], CeO_2 or

106   multiple Ce/Al/Zr additives [48], eutectic alkali chloride salts [49]; mechanical activation

107   [50,51]; thermal pre-treatments [52,53]; use of steam [54–56]. More recently, introduction of

108   inert materials in synthetic Ca-based sorbents has been scrutinized also with the aim of

109   improving their optical performance in terms of solar energy absorptivity, through the synthesis

110   of particles characterized by a darker colour [57–59]. While improving material stability, it was

111   recently found that the presence of inert compounds does not significantly affect the kinetics of

112   carbonation, and a slight modification of the parameters of the random pore model may be

113   sufficient to account for the presence of inert stabilizers [60]. Different process schemes have

114   been proposed and investigated in literature for integration between CSP and CaL for TCES.

115   Tregambi et al. [41] distinguished between open loop and closed loop conditions with respect

116   to CO_2. In the open loop condition, CaO carbonation is performed at 650 °C using a stream

117   coming from a CO_2 emitting industry, whereas calcination is performed at 850 °C using air,

118   and the produced stream is released to the atmosphere. Differently, in closed loop conditions,

119   calcination is performed at 940–950 °C under CO_2, that can then be recycled to the process.

120   Experimental tests performed in a FB heated by a solar simulator demonstrated that the harsher

121   conditions of closed loop during calcination induce a stronger loss of reactivity [41]. Castilla et

122   al. [61] investigated a process scheme for simultaneous TCES and CO_2 capture, and performed

123   a techno-economic analysis of the system. Sarrión et al. [62,63] proposed, instead, two different

124   process configurations for a closed loop CO_2 cycle for TCES. In both schemes, carbonation is

125   carried out at 850 °C under pure CO_2, to maximize the efficiency of the subsequent cycle for

126   energy production. Calcination is instead performed either at 750 °C under a N_2/He atmosphere

127   [62,63], or at 950 °C under pure CO_2 [63]. In the former case, use of membranes is proposed to

128   separate the produced CO_2 from the carrier gas and close the looping cycle. Experimental tests

129   have been performed only in a thermogravimetric analyzer, but proved again that harsher

130   conditions during calcination promote material sintering. The closed loop CO_2 scheme, with

131   carbonation/calcination at 850/950 °C under pure CO_2, has been investigated by model

132   computations also by Pascual et al. [64], who proposed the addition of a solid-solid separation

133   unit after the carbonator to separate converted and unconverted particles, thus avoiding the

134   looping of unreacted streams, to increase process efficiency. Since CaO carbonation to yield

135    $CaCO_3$ is generally proved to be a slow reaction step because of the time required for internal

136   CO_2 diffusion [60], it is reasonable to consider that unconverted streams may leave the

137   carbonator during continuous operation, thus supporting the usefulness/advantages of a Solid-

138   Solid Separation Unit (SSU). The feasibility of this operation is, however, still to be

139   demonstrated.

140   The aim of this study is to contribute to the existing knowledge on the CaL process for TCES,

141   by performing a dedicated experimental campaign under realistic process conditions suitable

142   for CaL-CSP integration, which are different from those typically investigated in literature for

143   carbon capture and storage. The closed loop CO_2 scheme, considering carbonation/calcination

144   at 850/950 °C under pure CO_2, has been selected because of its interesting features and because

145   of the lack of experimental data in apparatus different from thermogravimetric analyzers. In

146   this work, experimental tests were performed in FB reactors because of their peculiarity of

147   acting, simultaneously, as particle receivers for solar radiation and multiphase chemical

148   reactors. Decay of material reactivity and deactivation trend, as well as changes in

149   granulometric distribution of the bed inventory over cycling, were deeply scrutinized.

150   Attainable values of energy storage density were also computed. Moreover, the aim of

151 increasing the overall process efficiency of the process has been pursued by avoiding the
152 circulation of unreacted streams [64]. To this end, it was evaluated the possibility of separating
153 converted (i.e., $CaCO_3$-based) and unconverted (i.e., CaO-based) particles after the carbonation
154 step, exploiting the particle density difference. For the purpose, the minimum fluidization
155 velocity of calcined and carbonated particles was experimentally measured after each reaction
156 step at the relevant process temperature, to gather first data about the feasibility of this
157 operation. Finally, the influence of silica sand on the CaL performance, when experiments were
158 carried out using sand as ballast bed material, was highlighted.
159
160 **2. Process scheme**

161 The process plant devised for the closed loop CaL cycle for TCES is sketched in Figure 1. The
162 system entails two fluidized bed reactors (i.e., a solar calciner and a carbonator), three
163 intermediate Storage Tanks (STs) required to decouple collection and exploitation of solar
164 energy (i.e., one each for the calcined and carbonated material, one for the compressed CO_2), a
165 SSU at the exit of the carbonator, and several Heat Exchangers (HEs) for heat recovery or
166 preheating. A heat loss of 2% was assumed for each heat exchanger used for heat recovery.
167 Operation of the process is described in the following. More extent information of the
168 theoretical simulation of the CaL process as TCES is detailed by Pascual et al. [65]. A stream
169 of carbonated material (consisting of partially carbonated particles because of uncomplete
170 carbonation [41]) is fed from either the ST1 $CaCO_3$ storage tank (upon preheating from 200 to
171 850 °C through HE1) or from the carbonator itself to the calciner. Here, endothermic calcination
172 occurs driven by concentrated solar energy (100 MW energy input as reference case). Gaseous
173 atmosphere is 100% CO_2, therefore a process temperature of about 950 °C is required to
174 guarantee fast reaction kinetics. The stream of pure CO_2 exiting the reactor is partially recycled
175 as fluidizing gas to the reactor, and partially either sent to compression and ST3 (upon heat
176 recovery from 950 °C to 50 °C in HE3) or directly fed to the carbonator. The CO_2 is stored in
177 ST3 at 75 bar and 35 °C, after being previously compressed and cooled in 4 interleaved stages
178 (CCT in Figure 1). A pressure ratio of 3 was assumed for each of the four compression stages
179 to finally reach the CO_2 storage pressure (75 bar). The energy penalty associated to the
180 compression stages is the electrical energy consumption, rising to 8.41 MW maximum [65].
181 The first three cooled stages reduce the temperature to 50 °C and the fourth to the CO_2 storage
182 temperature (35 °C). The heat from the cooled stages is recovered, being the heat losses of 2%.
183 Similarly, particles leaving the calciner are sent to ST2 (upon heat recovery from 950 °C to 200

184   ºC in HE6), or directly to the carbonator. Finally, the calciner also processes an additional

185   stream of fresh limestone and purges a stream of spent material, which is required to

186   compensate for the decay of material reactivity over cycling ("chemical loss") and for the

187   elutriation of fine particles generated upon attrition/fragmentation phenomena ("physical loss")

188   [66]. The fresh limestone is fed at ambient temperature (25 ºC) and a heat recovery of the purged

189   spent material is done through HE8 from 950 ºC to 200 ºC. The calcination step is in operation

190   only upon availability of solar energy (ECL). When the collected solar energy needs to be

191   retrieved (ECR), CaO and CO_2 are fed to the carbonator either from the CaO/CO_2 storage tanks

192   (ST2 and ST3) (upon preheating through HE7 and HE5, respectively) or directly from the

193   calciner. The HE7 receives CaO streams from (i) calciner at 950 ºC and (ii) ST2 at 200 ºC to

194   be preheated to carbonator conditions (850 ºC). The HE5 preheats the CO_2 mixture from ST3

195   at 15 ºC and calciner at 950 ºC to 850 ºC. The CO_2 from ST3 suffers a discharging expansion

196   (DE in Figure 1) before being fed into HE5 at 15 ºC. Reactive atmosphere in the carbonator is

197   100% CO_2: carbonation is then performed at high temperature (850 °C) to maximize the

198   efficiency of the subsequent thermodynamic cycle for power production. The carbonation

199   reaction is generally a slow reaction step because of the time required for internal CO_2 diffusion.

200   Fluidized beds may be viewed as continuously stirred tank reactors in terms of solid residence

201   time distribution. Thus, it is reasonably to consider that the solid stream exiting the carbonator

202   includes both carbonated particles (consisting of both CaO and $CaCO_3$, mostly concentrated in

203   the core and shell of the particle, respectively) and unreacted (or less carbonated) particles.

204   Unreacted CO_2 stream is found at carbonator outlet given the uncomplete exothermic

205   carbonation reaction. The unreacted CO_2 from carbonator is sent to the CCT after a heat

206   recovery from 850 ºC to 50 ºC in HE4. The carbonator model applied for the theoretical CaL

207   TCES simulation was based on the kinetic model described by Grasa et al. [67] under carbon

208   capture conditions (650 ºC and 10-15%$_v$ of CO_2). A SSU is then implemented for the separation

209   of carbonated and unreacted particles: carbonated material is sent either to ST1 (upon heat

210   recovery from 850 ºC to 200 ºC in HE2) or to the calciner, whereas unreacted or less reacted

211   material is cycled back to the carbonator at 850 ºC, closing the looping cycle. To allow the

212   solid-solid separation, the SSU consists of a tapered fluidized bed reactor operated under

213   transient fluidization regime, so as to induce segregation of lower density particles to the top of

214   the column [68,69]. The inclusion of the total separation of carbonated and unreacted particles

215   was firstly proposed by Pascual et al. [64] to enhance the energy efficiency of the CaL TCES

216   system. Moreover, the effect of the SSU on the energy penalties and plant size reduction was

217   assessed under theoretical simulation. The threshold scenarios (no separation and total

218 separation of solids after carbonation step) were evaluated to provide information of the
219 maximum and minimum energy and size requirements. A size reduction between 53 and 74 %
220 was showed for heat exchangers affected by solid streams when the SSU is included [65].

221
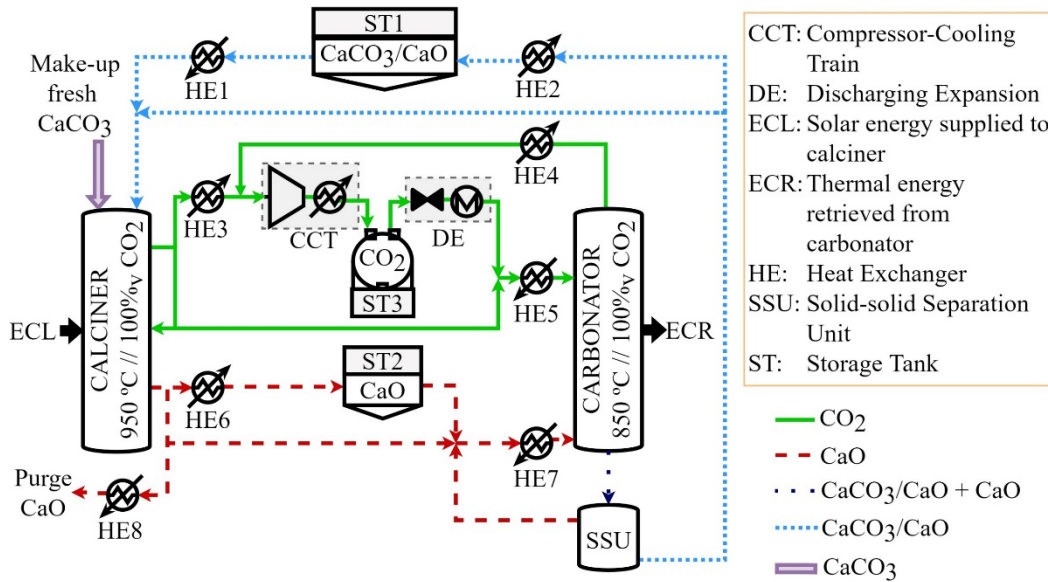
223 **Figure 1.** Simplified conceptual scheme for closed loop CaL-CSP integration, taken as reference in
224 this work.

225

226 **3. Experimental**

227 The experimental campaign consisted in CaL tests performed under operating parameters
228 relevant for the process integration outlined in the previous paragraph. Tests were performed
229 in semi-batch mode using a single FB reactor, by switching the process conditions between
230 carbonation and calcination. Two different experimental rigs were used for the whole
231 experimental campaign: i) a fluidized bed reactor equipped with a solar simulator, to mimic the
232 effect of concentrated solar radiation and estimate the decay of reactivity over cycling; ii) an
233 electrically heated fluidized bed reactor, to determine the changes in the particle properties
234 (granulometric distribution, porosity and density) of the bed inventory over cycling, as well as
235 the minimum fluidization velocity of the material after each reaction step.

236

237 *3.1 Experimental apparatus*

238 The FB reactor used for the CaL tests under solar simulated conditions is sketched in Figure 2.
239 The reactor has been used in previous experimental campaigns and a comprehensive description
240 of the experimental rig can be found in [41,52]. The FB reactor has an internal diameter of 0.1
241 m and, starting from the bottom, is made of three components: i) a windbox with an upper

perforated plate serving as gas distributor (0.5 mm holes on a triangular pitch); ii) a fluidized bed section, 0.1 m high; iii) a conical freeboard section (0.4 m high, internal cone angle of about 30°) with an upper optical window required to seal the reactor environment while allowing entrance of the concentrated solar radiation. At middle height of the conical section, four discharge ports (1 inch diameter) are provided for gas outlet. The reactor is heated by: i) a gas heater (manually controlled), able to heat the gaseous stream up to 700 °C; ii) two semicylindrical radiant heaters (driven by a PID controller) which surround the windbox and fluidized bed sections; iii) a solar simulator, made up by three 4 kW$_e$ short-arc Xe-lamps coupled with elliptical reflectors, able to produce a peak flux of about 3 MW m^{-2} and a total irradiated power of about 3.2 kW$_{th}$ on the bed surface. Electronic mass flow controllers are used for gas feeding to the reactor. Four K-type thermocouples are located within the system for temperature measurement: i) one at the exit of the gas preheater; ii) one within the windbox, 0.02 m below the distribution grid; iii) two inside the FB, 0.05 m over the distribution grid and 0.05 m from the reactor wall (middle thermocouple), and 0.08 m above the distribution grid and 0.01 m from the reactor wall (up thermocouple).
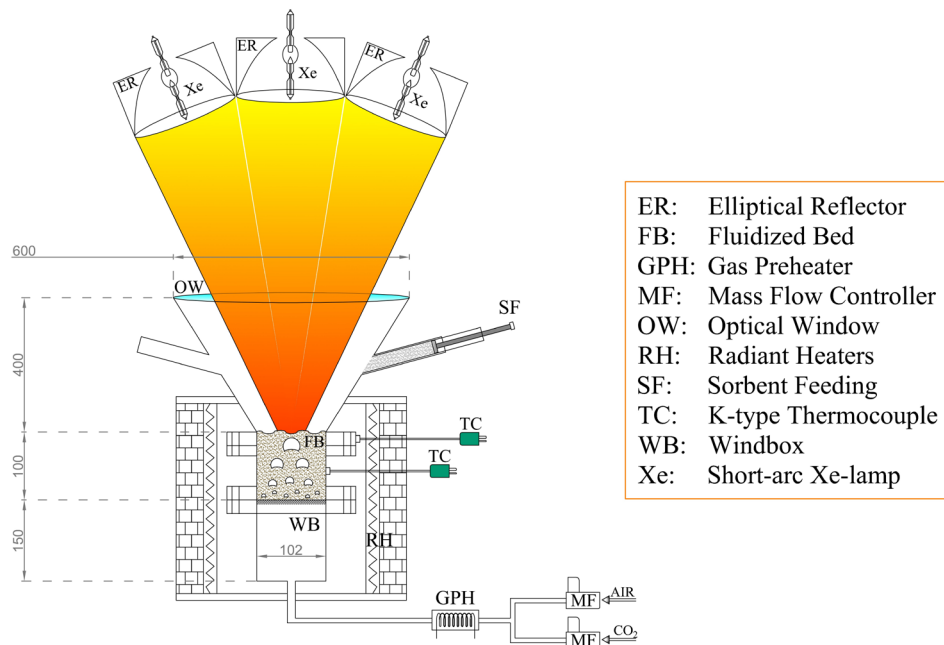

Figure 2. Directly irradiated fluidized bed reactor used in the present work. Dimensions in mm.

The electrically heated FB reactor is depicted in Figure 3. It features an internal diameter of 0.04 m and, starting from the bottom, is made of two components: i) a windbox section, 0.6 m high, with an upper stainless steel wire mesh serving as gas distributor; ii) a reaction plus freeboard section, 0.8 m high (the relative extension of the two zones depends on the bed

inventory). Exhaust gas leaves the reactor at the top of the freeboard. Two semicylindrical radiant heaters (driven by a PID controller) surround the reaction/freeboard zone and the windbox zone for an overall length of about 0.6 m. A lateral port, located a few millimeters above the distribution grid, is used for the simultaneous temperature and pressure measurement inside the FB reactor by a K-type thermocouple and a piezoelectric pressure transducer, respectively. Electronic mass flow controllers are used for gas feeding. The reactor is also equipped with a vacuum system to discharge and collect the bed inventory under cold or hot conditions.

FB:	Fluidized Bed
MFC:	Mass-flow Controller
PT:	Pressure Transducer
RH:	Radiant Heaters
TC:	K-type Thermocouple
WB:	Windbox
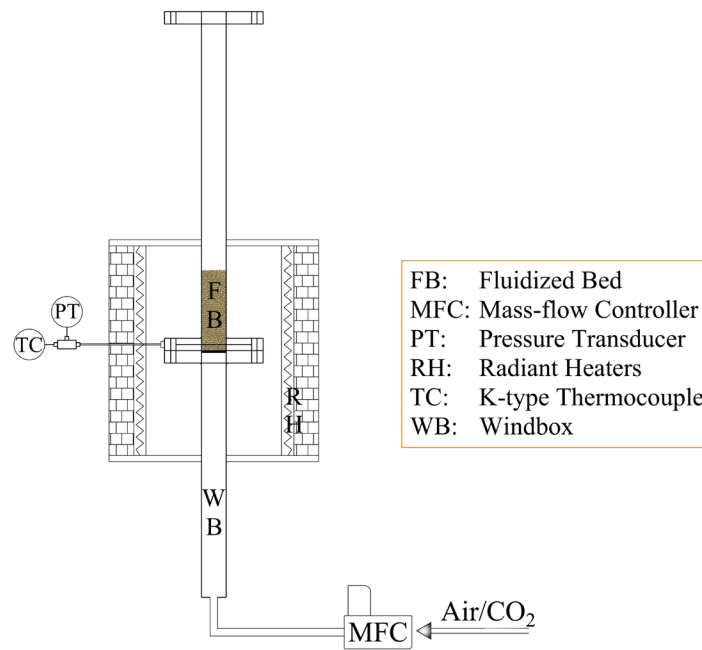
Figure 3. Electrically heated fluidized bed reactor used in the present work.

3.2 Materials

Two different materials were used in the experimental campaign: a silica sand from the Ticino river (Italy) and a natural Italian limestone, whose main properties summarized in Table 1. Besides SiO_2 (83.9%wt), the other constituents of the Ticino sand are Na_2O (1.8%wt), K_2O (2.4%wt), CaO (0.9%wt), MgO (1.0%wt), Al_2O_3 (8.4%wt), Fe_2O_3 (1.4%wt).

Table 1. Main properties of the materials used in the experimental campaign.

Material	Bulk density, tapped [kg m^{-3}]	Size range [μm]	CaO content (calcined material) [%wt]	u_{mf}^t (850–950 °C)* [m s^{-1}]

Limestone	1590	420–590	97.4	0.12–0.11
Ticino sand	1489	850–1000	0.9	0.35–0.33

284 * Minimum fluidization velocity, calculated according to Grace [70].

285

286 *3.3 Experimental conditions and procedure*

287 Regardless of the experimental rig, for all the CaL tests performed in this work the following

288 process parameters, relevant to closed loop CaL-CSP integration, were used:

    289   i)   reacting atmosphere of $100\%_v$ CO_2 during both carbonation and calcination;

    290   ii)   reaction time of 20 min for both reaction steps;

    291   iii)   superficial gas velocity of 0.6 m s^{-1} throughout the process;

    292   iv)   process temperature of 850 °C and 950 °C during carbonation and calcination,

293   respectively.

294 Moreover, for the experimental runs performed in the directly irradiated FB, bed inventory

295 consisted in a mixture of silica sand ($82\%_{wt}$) and limestone ($18\%_{wt}$). Silica sand acts as a thermal

296 flywheel, smoothing and mitigating the temperature variations induced by the chemical

297 reactions. This lime-to-sand ratio was used also in previous experimental campaigns [41,52],

298 and is retained in this work also for a better data comparison. Differently, for the experimental

299 runs performed in the electrically heated FB, bed inventory consisted in either a 1:1 mixture of

300 silica sand and limestone, or limestone only. The smaller scale of the plant allows indeed a

301 better temperature control, offering the possibility of working with higher percentage of lime.

302 This also permitted to perform different characterizations on the reactive material.

303

304 *3.3.1 Directly irradiated fluidized bed (Experimental Procedure #1)*

305 First, the system was charged with ~700 g of sand and heated up to 900 °C by the radiant and

306 gas heaters, using air as fluidizing gas. Once achieved this temperature, the fluidizing gas was

307 switched to CO_2 for 5 min to flush all the air from the reactor. Then, radiant heaters were

308 powered off, and a sample of 150 g of limestone was fed to the reactor. Then, the solar simulator

309 was turned on at the power required to keep the bed at 950 °C to perform the calcination step,

310 assuming as reference the "up" thermocouple. After 20 min (calcination reaction time), the

311 solar simulator was turned off, the fluidizing gas switched to air, and the radiant heaters turned

312 on with a set point temperature of 850 °C. The fluidizing gas was then switched back to CO_2,

313 to perform the carbonation step. After 20 min (carbonation reaction time), the radiant heaters

314 were turned off and the bed was heated up to 950 °C by means of the solar simulator, to perform

a new calcination step. The procedure was repeated until completion of 20 looping cycles. At the end of each carbonation step, a small sample of bed material (1–2 g) was collected for the subsequent determination of the carbonation degree of the sorbent. Sand and reactive material were separated by sieving.

Overall, the temperature control in the directly irradiated fluidized bed was quite satisfactory. During the calcination, after the initial transient heating to 950°C, the average temperature recorded by the up and middle thermocouple was 955 ± 4 °C and 968 ± 5 °C, suggesting a slight bed overheating. During the carbonation, the temperatures recorded by the up and middle thermocouples were in good agreement, with an average value of 838 ± 11 °C.

3.3.2 Electrically heated fluidized bed

Three different experimental procedures were carried out in this facility: a) to assess the sorption degradation of limestone under CaL TCES conditions; b) to assess the interaction of sand presence in limestone degradation under CaL TCES conditions; c) to estimate the minimum fluidization velocity of the calcined and carbonated material upon iterated cycles.

Experimental Procedure #2

The following experimental procedure was applied to those tests performed with a bed inventory of limestone only. First, the system was charged with ~180 g of sand and heated up to 900 °C using air as fluidizing gas. Once achieved this temperature, the vacuum system was used to discharge the bed inventory, and the reactor was cleaned to remove any trace of sand. The fluidizing gas was switched to CO_2, and flowed for 2 min to completely flush the air from the reactor. Then, a sample of 180 g of limestone was fed to the reactor and the PID controller was set to 950 °C to perform the calcination step. After 20 min, heating of the FB was stopped, and the bed inventory was collected by the vacuum system. Before this operation, the fluidizing gas was switched back to air, to prevent a possible sorbent re-carbonation induced by the temperature reduction. The collected material was cooled down to ambient temperature, and weighted. It was then estimated the bulk density of the sample, by pouring the material in a 50 mL graduated cylinder and measuring the weight and occupied volume. Finally, the sample was sieved in the following size ranges: 0–100 μm, 100–200 μm, 300–420 μm and 420–590 μm, and each granulometric cut was individually weighted. All the material was eventually mixed back and fed into the still hot FB reactor under air atmosphere. The PID controller was set to 850 °C and, once reached this temperature, the fluidizing gas was switched to CO_2 to perform the carbonation step. After 20 min, heating of the FB was stopped, and the bed

349 inventory was collected by the vacuum system under CO_2 atmosphere and cooled to ambient
350 temperature. Overall weight (required to evaluate the carbonation degree), bulk density and
351 granulometric distribution were determined as previously described. After that, the sample was
352 fed back to the FB reactor under CO_2 atmosphere, and the PID controller was set to 950 °C, to
353 perform a new calcination step. The procedure was repeated until completion of 20 looping
354 cycles. Overall, the temperature control in the electrically heated fluidized bed was quite
355 effective. During the calcination, apart from a brief overshoot of 10°C during the initial transient
356 heating to 950 °C, the average temperature was 950 ± 2 °C. Similar fluctuations were observed
357 during the carbonation, with an average temperature of 850 ± 2 °C.

358

359 *Experimental Procedure #3*
360 A different experimental run was also performed by applying the same experimental procedure
361 but using a bed inventory of sand and limestone (1:1 weight mixture). Material characterizations
362 were carried out after separation of the sorbent from the sand, performed by sieving. The first
363 calcination was however performed with limestone only, to produce a relevant amount of
364 material for the subsequent cycles.

365

366 *Experimental Procedure #4*
367 Finally, to estimate the minimum fluidization velocity, a different experimental run was
368 performed, using again a bed inventory of reactive material only. The same experimental
369 procedure described above was applied but, after each reaction step, the bed inventory was not
370 discharged. Instead, an automated script developed in LABVIEW was run to measure the
371 pressure drop vs. the superficial gas velocity in a "down-curve" from 30 to 0 cm s^{-1}, with 1 cm
372 s^{-1} step. Curves were acquired at the process temperature of the relevant step, using CO_2 as
373 fluidizing gas. Particular accuracy was dedicated to ensuring the temperature uniformity of the
374 entire fluidized bed when decreasing the superficial gas velocity. To this aim, the bed was
375 vigorously fluidized before the acquisition of each pressure drop measurement.

376

377 *3.4 Data analysis and further characterization*
378 The mean carbonation degree for the tests performed in the directly irradiated FB was evaluated
379 using the samples of carbonated material collected after each carbonation step. The samples
380 were individually calcined in a muffle furnace at 950 °C under air atmosphere, and the weight
381 change was measured with an analytical balance (0.1 mg precision), so as to determine the mean
382 carbonation degree as described in Di Lauro et al. [52].

383   For the tests performed in the electrically heated FB, the data of overall weight after each

384   reaction step were used to compute the mean carbonation degree ($\bar{X}_{Ca}$) as:

385
$$\bar{X}_{Ca}(N) = \frac{(m_N^{carb} - m_{N-1}^{calc})}{m_{N-1}^{calc} x_{CaO}} \frac{MW_{CaO}}{MW_{CO_2}} \tag{1}$$

386   where N is an index for the cycle number, m^{carb} and m^{calc} represent the overall weight of the

387   carbonated and calcined sample, respectively, x_{CaO} is the mass fraction of CaO in the calcined

388   sorbent (see Table 1), MW stands for molecular weight.

389   Mean carbonation degree data were further processed to compute the average energy storage

390   density (E_{SD}) following the methodology described in Di Lauro et al. [52]. Computed values

391   account for both the chemical heat and sensible heat contributions.

392   Data of Particle Size Distribution (PSD) were post-processed to evaluate the mean Sauter

393   diameter.

394   The curves of pressure drop vs. superficial gas velocity were analyzed to compute the minimum

395   fluidization velocity of the calcined and carbonated particles.

396   Finally, samples of lime retrieved after the last calcination step were subjected to X-Ray

397   Diffraction (XRD) analysis, performed using a Rigaku MiniFlex 600 instrument, and to

398   N_2-intrusion porosimetric analyses to investigate differences in specific surface area (through

399   BET theory), total pore volume and pore size distribution (through BJH theory).

400

401   **4. Results**

402

403   *4.1 Sorbent carbonation degree*

404   Figure 4 shows the mean carbonation degree of the sorbent obtained in the different

405   experimental tests (*EP #1*, *#2* and *#3*). It is possible to observe that the mean carbonation degree

406   decreases along with reaction cycles. Sintering phenomena and loss of reactivity are induced

407   by the high temperature and high CO_2 concentration experienced by the sorbent during both

408   reaction steps. With reference to experimental tests performed in the directly irradiated FB

409   (*EP#1* where solid inventory includes limestone and sand), $\bar{X}_{Ca}$ decreases from about 61%

410   (*N*=1) to about 4% (*N*=20), with an average value of 14% over the whole 20 reaction cycles.

411   Performance of the tests carried out in the electrically heated FB with a bed inventory of

412   limestone and sand (*EP #3*) do not differ sensibly: $\bar{X}_{Ca}$ decreases from about 60% (*N*=1) to about

413   8% (*N*=20), with an average value of 16% over the whole reaction cycles. The slightly worse

414   performance achieved in the directly irradiated FB may be caused by the overheating of the bed

415   surface induced by the highly concentrated solar radiation, as observed in previous research

416   studies [11]. The temperature difference between the "middle" and "up" thermocouple ranged

417   within 13.4 ± 3.2 °C across the different tests. The bed surface overheating was not measured

418   in this work, but according to previous experimental studies it can be as high as 80°C in the

419   centre of the FB [11,41]. Differently, the tests performed in the electrically heated FB with a

420   bed inventory of limestone only (*EP #2*) show better performance in terms of sorbent reactivity.

421   The mean carbonation degree decreases indeed from about 62% (1st cycle) to about 14% (20th

422   cycle), with an average value over the whole 20 cycles of about 25%. This was an unexpected

423   result that needed further investigation. In particular, it was scrutinized in literature a possible

424   chemical interaction between the silica sand constituents and lime particles, with the formation

425   of unreactive compounds, which can subtract reactive CaO, and induce a loss of reactivity.

426   Dicalcium silicate (Ca_2SiO_4, i.e. belite), one of the main constituents of the Portland cement

427   clinker [71,72], is formed when raw meals for cement production are used as sorbents in CaL

428   process for CO_2 capture [73]. It was claimed that its formation reduces the CO_2 sorption

429   capacity of the cement raw meals subtracting CaO sites available for the carbonation reaction

430   [74]. Valverde et al. [75] also observed the formation of calcium silicates from the interaction

431   of a calcium-based sorbent and a SiO_2 nanostructured powder under CaL conditions. However,

432   in this case the addition of nanostructured SiO_2 increases the carbonation degree improving the

433   CO_2 accessibility to the CaO sites. Experimental data plotted in Figure 4 shows a detrimental

434   effect of Ticino silica sand on lime reactivity, in analogy with the findings obtained with cement

435   raw meals used in CaL process for CO_2 capture [73]. A further consequence of this result is

436   related to the use of additives, devoted to improve the fluidizability of small particles of

437   limestone and/or to improve its optical performance in terms of absorption of concentrated solar

438   energy. Their addition to sorbent particles should be carefully evaluated because of possible

439   interaction with lime and consequent decrease in reactivity.

440
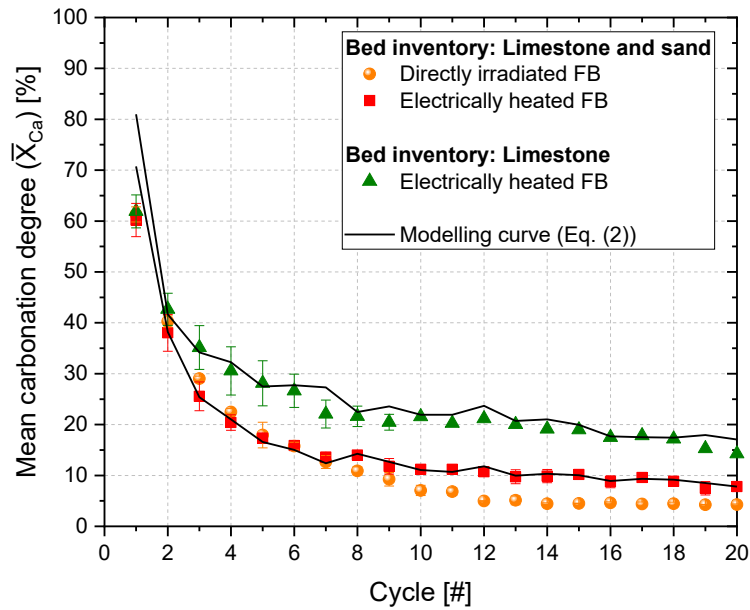
Figure 4. Mean carbonation degree of the sorbent as a function of the cycle number and of the adopted operating conditions.

Post-processing of $\bar{X}_{Ca}(N)$ data has been carried out by postulating here the following IAD "Initial Activity Decay" equation:

$$\bar{X}_{Ca}(N) = k_1 N^{-k_2} \tag{2}$$

where k_1 is the initial activity constant, that measures the efficacy of the sorbent when $N=1$ ($\bar{X}_{Ca}(N=1) = k_1$), and k_2 is the decay constant that considers the resistance of the sorbent to sintering phenomena (the higher k_2, the worst the sintering resistance). While Figure 5 shows data fitting, Table 2 lists the best-fitting values for k_2 (along with the values for the coefficient of determination). Sintering resistance for the sorbent in the case of limestone inventory and electrically heated FB (*EP #2*) resulted ca. 33% and 49% higher vs. the cases with limestone and sand inventory (electrically heated (*EP #3*) and directly irradiated FB (*EP #1*), respectively), to confirm the ranking discussed above.

458
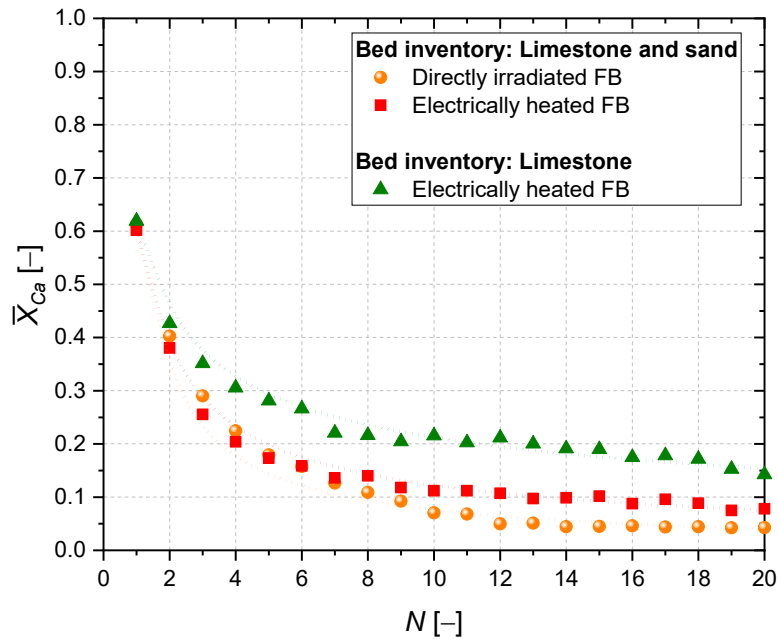
459 **Figure 5.** Fitting of experimental carbonation degree data by the IAD Eq. (2).

460

461 **Table 2.** Values for the decay constant (IAD model) for the cases under investigation.

	k_2 [–]	R^2 [–]
Limestone and sand inventory Directly irradiated FB	0.91	0.97
Limestone and sand inventory Electrically heated FB	0.69	0.98
Limestone inventory Electrically heated FB	0.46	0.97

462

463 *4.2 Density of energy storage*

464 Figure 6 shows the average values of energy storage density up to the reaction cycle considered

465 vs. reaction cycle, for the different experimental runs. Data were computed under a conservative

466 scenario by considering the loose density of limestone, which is about 13% lower than the

467 tapped density value [52]. The energy storage density of the molten salts is also plotted as

468 reference material, though a more comprehensive comparison should also account for the

469 different technology and operating conditions of the two processes (i.e., thermal energy storage

470 with molten salts and TCES with CaL). For the tests with a bed inventory of limestone and

471 sand, the average values of E_{SD} are quite similar for the two experimental rigs and decrease

472 from about 1550 MJ m^{-3} (1 looping cycle) to 485 MJ m^{-3} (20 looping cycles). Under these

473 process conditions, the CaL system outperforms the molten salts one only up to an average

474 sorbent life of 6 cycles. From the 8th cycle onwards, the molten salts system appears to be

superior. Data obtained in this study appear to be worse than those shown in Di Lauro et al. [52] for limestone in closed loop configuration, where carbonation was performed at 650 °C and 15%$_v$ CO_2. This arises because of: i) a slightly lower reactivity of the sorbent in the present study, probably induced by the higher temperature and CO_2 concentration experienced during carbonation (mean carbonation degree at the 20th reaction cycle is of 13.7% in this work vs. 15.3% in Di Lauro et al. [52]); ii) a lower amount of sensible energy storage in this work (to perform carbonation, CaO is cooled from 950 °C to 850 °C in this work and from 950 °C to 650 °C in Di Lauro et al. [52]). Data of E_{SD} obtained with a bed inventory of limestone only are slightly better, especially at increasing looping cycles. Values decrease from about 1575 MJ m^{-3} (1 looping cycle) to 710 MJ m^{-3} (20 looping cycles). Even if the performance in terms of E_{SD} is comparable to that of molten salts when an average sorbent life of 10–20 cycles is considered, it should be recalled that, in this CaL process, thermal energy at the carbonator is released at a much higher temperature (i.e., 850 °C), with a consequent higher overall efficiency in the subsequent thermodynamic cycle for energy production. Moreover, the share of chemical heat storage over the total is very high. It values about 91% at the first cycle for all the tests, and decreases to 79% (10 looping cycles) and 70% (20 looping cycles) for the tests performed with a bed inventory of lime and sand, and to 84% (10 looping cycles) and 80% (20 looping cycles) for the tests performed with a bed inventory of limestone only.
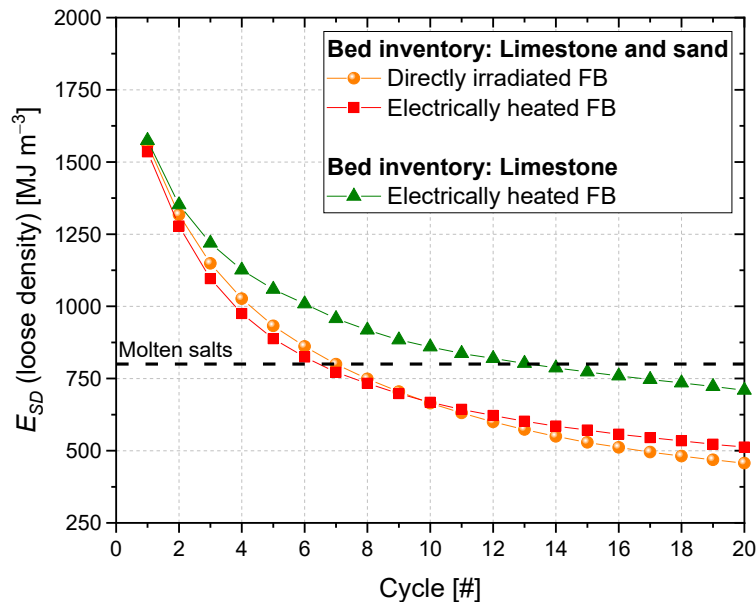

Figure 6. Average energy storage density up to the reaction cycle considered vs. reaction stage, under the adopted operating conditions.

497   *4.3 Particle size distribution*

498   Figure 7 shows information on the attrition/fragmentation of the bed inventory for the

499   experimental runs performed in the electrically heated FB. Data are plotted either as cumulative

500   PSD for selected calcination stages (Figure 7-A) or as mean Sauter diameter (d_{Sauter}) vs. reaction

501   number (Figure 7-B).

502   Figure 7-A highlights a progressive fragmentation/shrinkage of limestone particles along with

503   reaction cycles. Particles mostly shift from the 420–590 μm to the 300–400 μm size range,

504   whereas the mass fraction of smaller size ranges (< 300 μm) only slightly increases. The effect

505   is more pronounced for the tests performed with a bed inventory of limestone and sand,

506   suggesting that the presence of sand enhances the fragmentation/shrinkage of limestone

507   particles. Particle size reduction appears to be mostly concluded at the 10th calcination for tests

508   with a bed inventory of limestone only, as the PSD for the 10th and 20th calcined samples mostly

509   overlap. Differently, when the bed inventory of limestone and sand is used, the PSD for the 10th

510   and 20th calcined samples still shows significant differences. Discussed data are further

511   confirmed by the trend of d_{Sauter} highlighted in Figure 7-B. Starting from the 505 μm value of

512   the limestone samples fed to the reactor, d_{Sauter} decreases to about 475 μm and 425 μm for the

513   tests with a bed inventory of limestone only and limestone and sand, respectively. With regards

514   to tests with limestone only, the value of 475 μm is approached already at the 10th reaction step

515   (corresponding to the 5th carbonation). Differently, tests with a bed inventory of limestone and

516   sand show a first stabilization of d_{Sauter} at about 450 μm from the 10th reaction step on, followed

517   by a second decrease towards 425 μm from the 30th reaction step on, which suggests a further

518   weakening/shrinkage of the material structure upon iterated reaction cycles. Figure 7 also

519   highlights that, in both tests, the fraction of material below 150 μm is mostly negligible, as it

520   always accounts for less than 1%. It is reasonable that finer particles are also formed during the

521   process, but are elutriated from the system. For this reason, the make-up stream of fresh

522   limestone used in the process (see Figure 1), should be intended to also compensate for this net

523   mass loss [66].

524
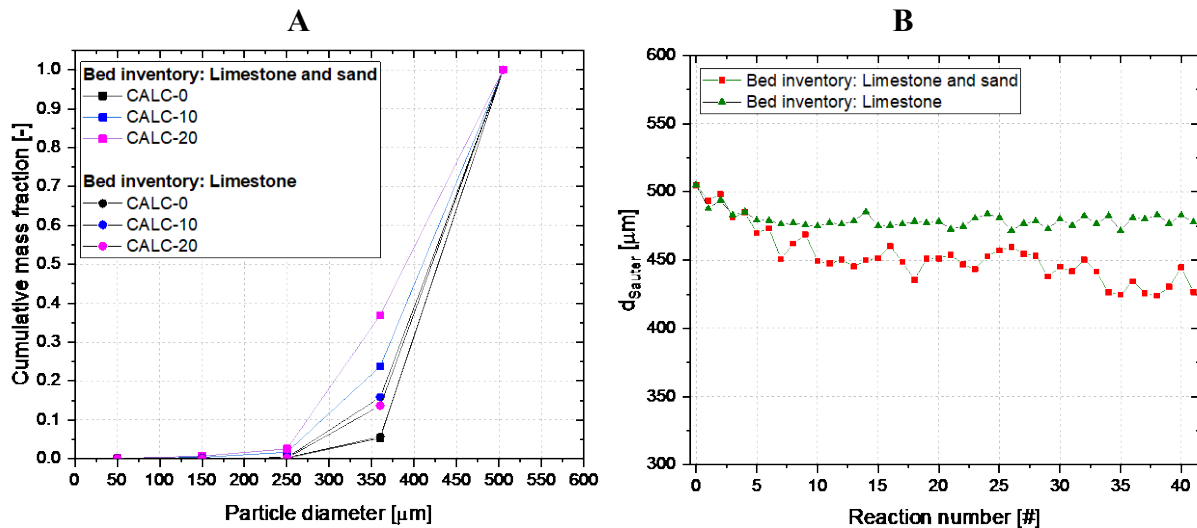
Figure 7. A) Cumulative particle size distribution for selected calcination stages (CALC-0 refers to the samples after the initial calcination); B) Mean Sauter diameter of the bed inventory vs. reaction number (reaction number 0 refers to the starting limestone samples).

4.4 Particle density

Figure 8 shows the bulk density of limestone particles after each reaction step for the tests performed with the bed inventory of limestone and sand and limestone only. As expected, the density values of calcined particles are always lower than those of the corresponding carbonated ones. However, the trend of density with reaction stage quite differs for the two experimental tests. Indeed, in tests with sand, the density of the calcined particles increases along with reaction cycles, whereas that of the carbonated particles is mostly constant after a decrease during the very first cycles. Differently, in tests without sand, the density of the calcined particles is mostly constant after an increase during the first reaction cycles, whereas that of the carbonated particles decreases along with the reaction cycles, especially during the first 8 carbonation steps. Further, for both carbonated and calcined particles, the density values obtained in tests with sand are always higher than those obtained in tests without sand. Data obtained when working with the bed inventory of limestone only are probably the easiest to explain: the density of carbonated samples decreases with reaction cycles because of the lower carbonation degree as the number of cycles progresses, whereas the density of calcined samples is mostly constant after a first increase resulting upon loss of porosity. Differently, data obtained when working with sand show that the density of the calcined samples increases because of the interaction with sand, whereas that of the carbonated samples remains mostly constant because the decrease induced by the lower carbonation degree is offset by the increase induced by the interaction with sand. This explanation is further corroborated by the higher density values

550 detected in tests with sand. Data were post-processed to evaluate the density increase that could

551 have been induced from belite formation, quantitatively evaluated on the basis of the reduction

552 of carbonation degree [73,74] with respect to the tests without sand. It was found that the

553 formation of belite can only justify an increase of 5% of materials density. It is noteworthy that

554 the sand may also physically act on the sorbent particles reducing their porosity and, in turn,

555 increasing the particle density of both calcined and carbonated samples.

556 The bulk density of the calcined and carbonated samples upon iterated cycles has been further

557 worked out to better correlate the physical properties of the granular solids along the course of

558 the CaL process. In particular, the obtained data can be used to estimate the mean conversion

559 degree during the carbonation step, and the particle density and porosity of the calcined and

560 carbonated samples, upon calcination/carbonation iterated cycles.

561 The mean carbonation degree can be calculated exclusively by the bulk density of batches of

562 calcined and carbonated particles once it is assumed that the volume occupied by the granular

563 solids does not significantly change during each single carbonation step. Equation (1) can then

564 be rearranged as:

565
$$\bar{X}_{Ca}(N) = \left(\frac{\rho_N^{carb} V_N^{carb} - \rho_{N-1}^{calc} V_{N-1}^{calc}}{\rho_{N-1}^{calc} V_{N-1}^{calc}}\right) \frac{MW_{CaO}}{x_{CaO} MW_{CO_2}} \approx \left(\frac{\rho_N^{carb}}{\rho_{N-1}^{calc}} - 1\right) \frac{MW_{CaO}}{x_{CaO} MW_{CO_2}} \qquad (3)$$

566 where ρ^{carb} and ρ^{calc} are the bulk density of the carbonated and calcined particles, respectively,

567 and V^{carb} and V^{calc} represent the volume occupied by the bed of carbonated and calcined

568 particles, respectively. The results obtained from Eq. (3) are reported in Figure 4 and, thereby,

569 compared with the conversion degree calculated by Eq. (1). The comparison highlights that the

570 method based on the measurements of bulk densities accurately agrees with the data obtained

571 from samples weight. This result can be used to set up alternative methods to estimate the

572 conversion degree during the carbonation step in, even large-scale, CaL systems, simply

573 sampling the granular solids both first and after each carbonation step.

574 The particle density of the calcined and carbonated materials at a generic N cycle, ρ_{pN}^{calc} and

575 ρ_{pN}^{carb}, respectively, can be estimated from the corresponding bulk densities by the following

576 equations:

577
$$\rho_{pN}^{calc} = \frac{\rho_N^{calc}}{1 - \varepsilon_{bedN}^{calc}}; \qquad\qquad \rho_{pN}^{carb} = \frac{\rho_N^{carb}}{1 - \varepsilon_{bedN}^{carb}} \qquad (4)$$

578 where $\varepsilon_{bedN}^{calc}$ and $\varepsilon_{bedN}^{carb}$ are the bed voidage during the bulk density measurement for the

579 calcined and carbonated materials at a generic N cycle, respectively. Assuming a constant bed

580 voidage equal to 0.41, a typical value for packed bed, the particle density can be easily

581 evaluated, and the obtained data points can be read in Figure 8 together with the bulk density

582 values.

583
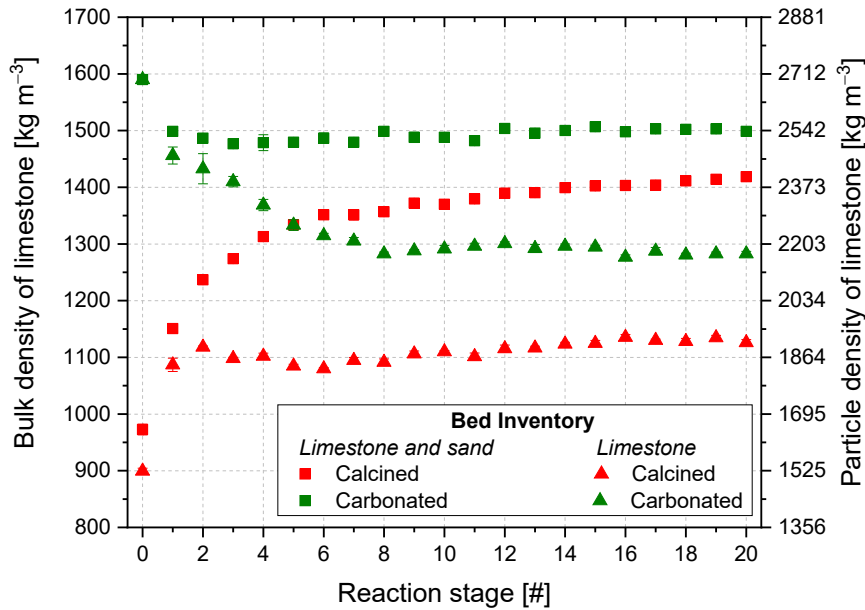
Figure 8. Bulk and particle density of limestone particles for calcined and carbonated samples, in tests performed with a bed inventory of limestone and sand, and limestone only.

587

588 The particle porosity of the calcined and carbonated particles, in turn, can be calculated by the

589 following equations, assuming as reference the density of pure CaO for the calcined particles,

590 and a mean value (based on the carbonation degree) between the density of pure CaO and

591 CaCO$_3$, for the carbonated particles:

$$\varepsilon_{pN}^{calc} = 1 - \frac{\rho_N^{calc}}{\rho_{CaO}}; \qquad \varepsilon_{pN}^{carb} = 1 - \frac{\rho_N^{carb}}{\frac{\overline{X}_{Ca(N)}MW_{CaCO_3}+(1-\overline{X}_{Ca(N)})MW_{CaO}}{\frac{\overline{X}_{Ca(N)}MW_{CaCO_3}}{\rho_{CaCO_3}}+\frac{(1-\overline{X}_{Ca(N)})MW_{CaO}}{\rho_{CaO}}}} \qquad (5)$$

593 where ρ_{CaO} and ρ_{CaCO_3} are the density of pure CaO and CaCO$_3$, set equal to 3340 kg m^{-3} and

594 2710 kg m^{-3}, respectively. It is worth to note that the contribution of solid compounds, formed

595 by the chemical interaction between lime and silica sand, to the absolute particle density has

596 been neglected.

597 Finally, it can be defined as "reactive" the porosity that vanishes during the carbonation step

598 as:

$$\varepsilon_{pN}^{react} = \varepsilon_{pN-1}^{calc} - \varepsilon_{pN}^{carb} \qquad (6)$$

The "reactive" porosity represents the internal porosity of the particles, which is occupied by the CO_2 molecules reacting with CaO to form $CaCO_3$ during the carbonation step. The particle porosity and the "reactive" porosity are shown as a function of the reaction stage in Figure 9 for all the investigated conditions.

Data in Figure 9-A counter-mirror those of Figure 8. The analysis of the data of particle porosity for the samples obtained processing only limestone particles highlights, as also reported in literature [76], that the reduction of reactivity of limestone is due to the reduction of porosity of the calcined particles during the first cycles, and the concurrent sintering of the carbonated particles along the iterated cycles. The porosity of carbonated particles increases upon iterated cycles in agreement with a larger amount of porosity no more accessible by CO_2 molecules during carbonation. A different scenario appears when analyzing the experimental data of the tests carried out using limestone with silica sand particles. The interaction with silica sand particles strongly influences the phenomenology: the porosity of calcined particles steadily decreases along the iterated cycles, whereas the porosity of carbonated particles increases only during the first cycles. Moreover, in presence of sand, particle porosity values are remarkably lower than the corresponding ones in the case without sand, Figure 9-B. The "reactive" porosity trend along iterated cycles confirms what already observed, and highlights a difference in the "reactive" porosity of about 0.04 in favour of the only limestone case.
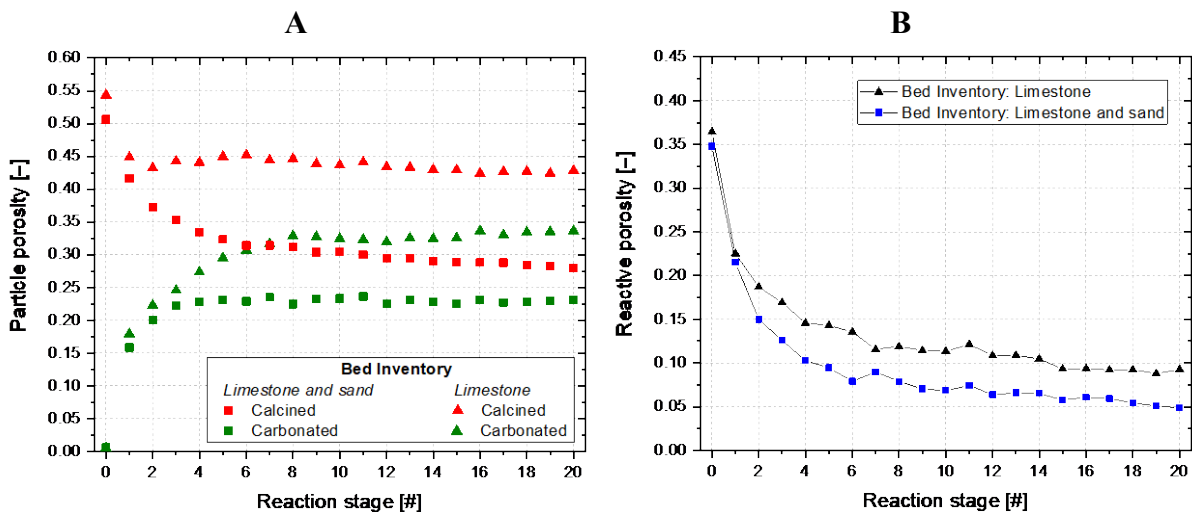
Figure 9. Particle (A) and "reactive" (B) porosity of limestone particles for calcined and carbonated samples in tests performed with a bed inventory of limestone and sand, and limestone only.

623 *4.5 XRD and visual analyses*

624 Figure 10 shows the XRD profiles of the lime samples retrieved after the last calcination step

625 for the tests performed in the electrically heated FB, together with that of pure sand. It is

626 possible to observe that:

627 - the XRD spectrum of the sand exhibits several characteristics peaks of quartz (SiO_2),

628   and a few minor peaks related to other compounds and impurities present in the sample;

629 - the XRD spectrum of the calcined sample retrieved from the tests performed with a bed

630   inventory of limestone only exactly matches the crystalline signature of lime (CaO);

631 - the XRD spectrum of the calcined sample retrieved from the tests performed with a bed

632   inventory of limestone and sand exhibits, apart from the peaks related to lime, several

633   additional peaks that match either those of quartz, or those of the other compounds

634   found in the sand.

635 XRD data seems to rule out a bulk chemical interaction between sand and lime since no peaks

636 related to new crystalline phases were detected. It is likely that a potential chemical interaction

637 takes place only at the particle surface, given the sizes of sorbent and sand particles used in this

638 study. For the sake of completeness, it should be underlined that sand-derived peaks found in

639 the calcined sample may arise, apart from very fine sand particles trapped in the lime pores,

640 also from sand particles that, upon iterated attrition/fragmentation, approached the size of lime

641 ones and were thus not trapped by the sieves. A quantitative XRD analysis was also performed

642 to assess the extent of sand contamination, and of belite formation. Belite formation was again

643 not detected while the sand percentage turned out to be 5–6%. Such low values cannot justify

644 the density differences observed in the two samples, and support the discussion on the reduction

645 of particles porosity previously highlighted (see §4.4).

646
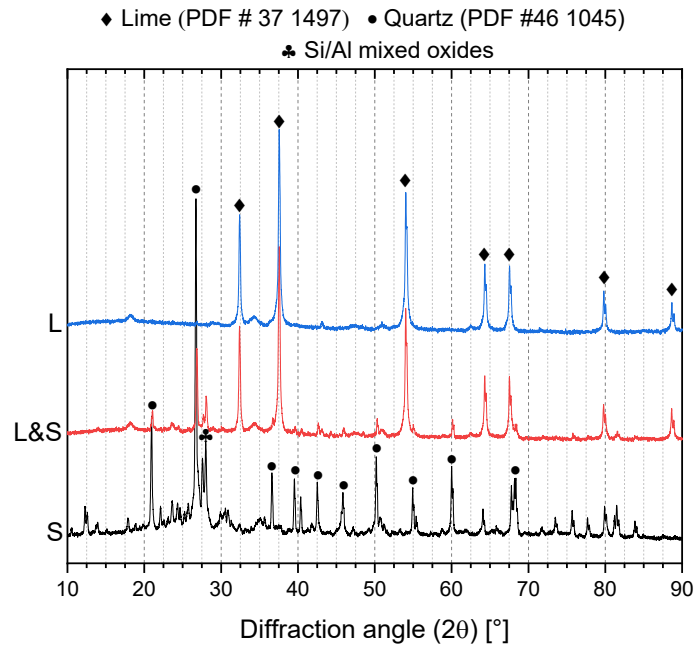
Figure 10. XRD profiles of: lime samples retrieved after the last calcination step in the electrically heated FB, for tests performed with a bed inventory of limestone only (L) and limestone and sand (L&S); pure sand (S).

Figure 11 shows a picture of these three samples. The comparison highlights that lime particles retrieved from the test performed with a bed inventory of sand and lime features a slightly darker colour, probably as a consequence of the physical and chemical interaction with the sand.


L **L&S** **S**

Figure 11. Picture of: lime samples retrieved after the last calcination step in the electrically heated FB, for tests performed with a bed inventory of limestone only (L) and limestone and sand (L&S); pure sand (S).

4.6 Porosimetric analyses

The results of the porosimetric analyses reveal that that the specific surface is quite low in all the samples (1–2 m^2 g^{-1}) calcined at the 20th cycle, and similar to values reported in other studies under severe calcination conditions [41]. The cumulative pore volume distribution of the different samples is, instead, shown in Figure 12. The lime sample processed in the electrically heated FB without sand, that is the best in terms of mean carbonation degree, is characterized by the highest value of total pore volume (0.165 cm^3 g^{-1}), mostly of which are mesopores (~88%). When lime is processed together with sand, the distribution is quite different depending on the reactor used. Lime processed in the electrically heated FB, that has intermediate performance in terms of mean carbonation degree, has the lowest value of total pore volume (0.047 cm^3 g^{-1}) but a significant share of both micropores and smaller mesopores (~80%), probably formed due to the sand/sorbent interaction. Differently, lime processed in the directly irradiated FB, that has the worst performance in terms of mean carbonation degree, has an intermediate value of total pore volume (0.106 cm^3 g^{-1}), but half of them are macropores and are thus less relevant for the reactivity of the material. The formation of larger pores may have been induced by the thermal sintering due the bed surface overheating produced by the simulated solar radiation. It seems that the sand/sorbent interaction might have played a less important role in these tests, probably due to the different hydrodynamics related to the larger scale of the used reactor.
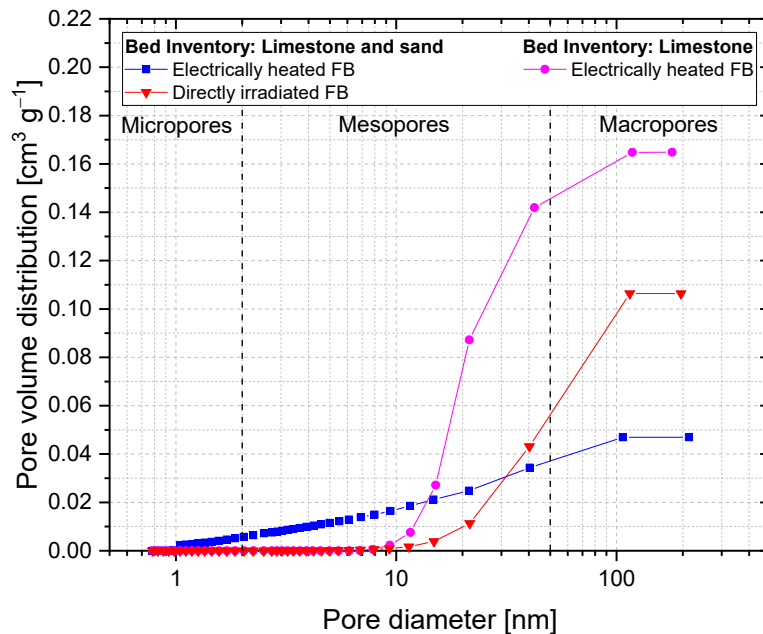
Figure 12. Cumulative pore volume distribution of the different samples, after the last calcination step.
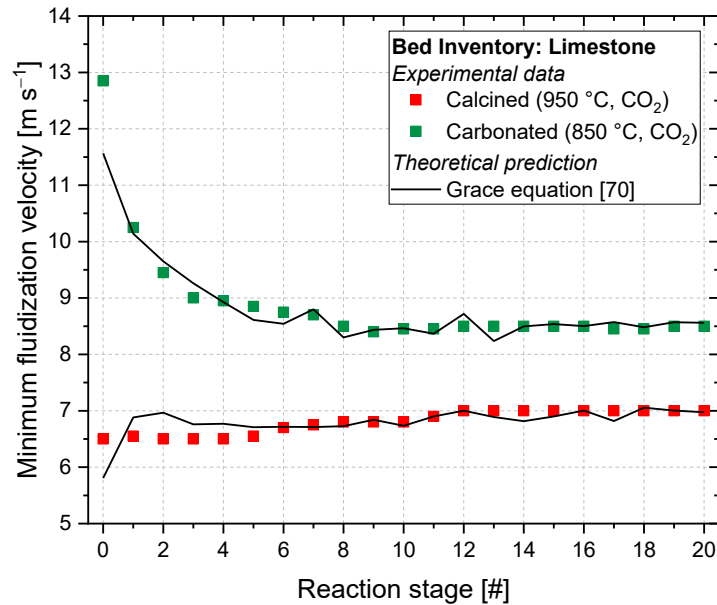
684 *4.7 Minimum fluidization velocity*

685 Figure 13 shows the minimum fluidization velocity of carbonated and calcined samples in tests

686 performed using a bed inventory of limestone only (*EP #4*). It is recalled that data were acquired

687 at the process temperature of the reaction step (i.e., 850 °C for carbonation, 950 °C for

688 calcination), using CO_2 as fluidizing gas. The trend of the minimum fluidization velocity recalls

689 that of the bulk density (see Figure 8). For calcined samples, the minimum fluidization velocity

690 slightly increases from an initial value of about 6.5 cm s^{-1} (initial calcination) to about 7 cm s^{-1}

691 (20th reaction stage). Conversely, for carbonated samples, the minimum fluidization velocity

692 decreases from about 10.2 cm s^{-1} (1st reaction stage) to about 8.5 cm s^{-1} (20th reaction stage).

693 Overall, a difference between the minimum fluidization velocity of carbonated and calcined

694 samples of about 3.7 cm s^{-1} can be inferred for more reactive particles, which decreases to about

695 1.5 cm s^{-1} for less reactive ones. The obtained experimental data were compared with those

696 calculated by the semi-empirical correlation proposed by Grace (Eq. (7)) [70]:

697
$$\frac{d_p u_{mf} \rho}{\mu} = \left[27.2^2 + 0.0408 \cdot \frac{d_p^3 \rho (\rho_p - \rho) g}{\mu^2}\right]^{1/2} - 27.2 \qquad (7)$$

698 where d_p is the particle diameter, u_{mf} the minimum fluidization velocity, ρ and ρ_p the gas and

699 particle density, respectively, μ the dynamic gas viscosity, and g the gravitational acceleration.

700 Particle size and density data used in Eq. (7) are those reported in Figures 7-B and 8,

701 respectively. The comparison shows a very satisfactory agreement, confirming the approach

702 proposed with Eq. (4). According to these data, it could be speculated that a solid-solid fluidized

703 bed separation may be feasible at least to some extent, to separate the more reacted particles

704 from the less reacted ones. The exploitation of a fluidized bed classifier, already proposed in

705 literature [68], could be explored for an efficient separation of the investigated granular solids.

706

Figure 13. Minimum fluidization velocity for calcined and carbonated sorbent samples at the relevant process temperature, using CO_2 as fluidizing gas, obtained from experimental data and theoretical approach.

5. Discussion

On the whole, the analysis of the experimental results discussed in the present work returns two key findings.

Co-processing of limestone with silica sand reduces the lime reactivity, as inferred from the lower values of mean carbonation degree. Post-process of density data, together with N_2-intrusion porosimetric analysis, and quantitative and qualitative XRD analyses, suggests that this effect is mainly due to a lime/sand mechanical interaction that induces a strong reduction of the total and reactive sorbent porosity. A chemical interaction between CaO and silica sand constituents, not detected by XRD analysis, might only occur at particle surface and to a small extent, and could not justify alone the decay of reactivity observed when coprocessing lime with silica sand. The detrimental effect of this interaction on the CaL performance poses concerns to the use of additives to improve the fluidizability of small particles of limestone and/or to improve its optical performance in terms of absorption of concentrated solar energy. Under the tested conditions, the density of energy storage becomes lower than that of the molten salts after 7 reaction cycles, even if the energy is retained in a more stable form and can be released at higher temperatures. Using a bed of only limestone may produce better results, but requires the design of the receiver as a blackbody cavity. In this case, the density of energy storage is only slightly lower than that of molten salts after 20 cycles that is the average sorbent life of the reactive material in the CaL process. According to these findings, it is advised to

731   consider materials different from sand, if additives need to be used. Alternatively, synthetic or

732   natural sorbents different from conventional limestone, and characterized by a better absorption

733   of solar energy [57–59,77], should be considered.

734   Carbonated and calcined particles are characterized by a different density and porosity, that

735   results into a sufficient difference in their minimum fluidization velocity. This difference may

736   be exploited for the design of a fluidized bed classifier that recycles unreacted or less reacted

737   particles to the carbonator. In this way, it would be possible to maximize the efficiency of the

738   process by ensuring the maximum carbonation degree of sorbent particles, and by avoiding the

739   circulation of streams of unreacted particles through the plant. It is noteworthy that the effective

740   advantage brought by the classifier is strictly related to the material reactivity and resistance to

741   sintering over cycling. When the reactivity of the material abruptly decreases over cycling the

742   efficacy of the classifier is probably lower, as the increase in conversion degree that could be

743   obtained from the material recycling is smaller. However, synthetic sorbents feature a much

744   stronger resistance to sintering, and are able to preserve better their initial reactivity over

745   cycling. In this case, the contribution of the classifier to the overall process efficiency may be

746   much higher.

747   Further tests will be performed in future works to fully demonstrate the feasibility and

748   efficiency of the FB classifier, and to estimate its contribution to the overall efficiency of the

749   process. Moreover, different inert materials will be tested in mixture with lime, and in different

750   ratio, to scrutinize their potential advantages and drawbacks in the CaL process for TCES.

751

752   **Conclusions**

753   The calcium looping process integrated with TCES has been investigated focusing the attention

754   on the closed loop CO_2 scheme with carbonation/calcination at 850/950 °C under pure CO_2. In

755   particular, the conditions needed for the addition of a solid-solid separation unit after the

756   carbonator to separate converted and unconverted particles and, consequently, to increase the

757   process efficiency, have been analyzed. The experimental tests, performed in the directly

758   irradiated FB, show that the mean carbonation degree decreases from about 61% (1st cycle) to

759   about 4% (20th cycle), with an average value of 14% over the whole 20 reaction cycles. Similar

760   results are obtained in the electrically heated FB with a bed inventory of limestone and sand.

761   Differently, the tests performed in the same reactor with a bed inventory of limestone show

762   superior performance: the mean carbonation degree decreases indeed from about 62% (1st

763   cycle) to about 14% (20th cycle), with an average value over the whole 20 cycles of about 25%

764   (data were confirmed by evaluation of the deactivation constant, obtained by the application of

an initial activity decay equation). It seems that the chemical interaction of CaO with the silica sand constituents at the process temperatures is not the main responsible for the loss of reactive CaO toward CO_2 uptake. Instead, post-process of particle density data, together with N_2-intrusion porosimetric analysis, and quantitative and qualitative XRD analyses, suggests that the sand/lime mechanical interaction induces a strong reduction of the total and reactive sorbent porosity that is the main responsible for the strong decay of reactivity. The detrimental effect of this interaction on the calcium looping performance poses concerns to the use of additives to improve the fluidizability of small particles of limestone and/or to improve its optical performance in terms of absorption of concentrated solar energy. For the tests with a bed inventory of limestone and sand, the average values of energy storage density are quite similar for the two experimental rigs and decrease from about 1550 MJ m^{-3} (1 looping cycle) to 485 MJ m^{-3} (20 looping cycles). Instead, with a bed inventory of limestone, the values decrease from about 1575 MJ m^{-3} (1 looping cycle) to 710 MJ m^{-3} (20 looping cycles). The performance in terms of energy storage density is comparable to that of molten salts when an average sorbent life of 10–20 cycles is considered. However, it should be recalled that, in this CaL process, thermal energy at the carbonator is released at a much higher temperature (i.e., 850 °C), with a consequent higher overall efficiency in the subsequent thermodynamic cycle for energy production. The main properties of calcined and carbonated particles significantly change in terms of particle density, size and porosity, if the limestone is processed with silica sand fluidized particles. Finally, the measurements of minimum fluidization velocity of calcined and carbonated particles upon iterated cycles of calcination and carbonation show that a solid-solid separation based on particle density difference may be conceived by a fluidized bed classifier already proposed in literature [68].

References

[1]   H. Zhang, H. Benoit, I. Perez-Lopèz, G. Flamant, T. Tan, J. Baeyens, High-efficiency

solar power towers using particle suspensions as heat carrier in the receiver and in the thermal energy storage, Renew. Energy. 111 (2017) 438–446. doi:10.1016/j.renene.2017.03.101.

[2] C. Tregambi, S. Padula, M. Galbusieri, G. Coppola, F. Montagnaro, P. Salatino, M. Troiano, R. Solimene, Directly irradiated fluidized bed reactor for thermochemical energy storage and solar fuels production, Powder Technol. 366 (2020) 460–469. doi:10.1016/j.powtec.2020.02.045.

[3] C.K. Ho, Advances in central receivers for concentrating solar applications, Sol. Energy. 152 (2017) 38–56. doi:10.1016/j.solener.2017.03.048.

[4] A. Bayon, A.J. Carrillo, E. Mastronardo, J.M. Coronado, Chapter Six - Thermochemical heat storage at high temperature, in: W. Lipiński (Ed.), Sol. Thermochem., Academic Press, 2021: pp. 247–295. doi:https://doi.org/10.1016/bs.ache.2021.10.004.

[5] A.J. Carrillo, J. González-Aguilar, M. Romero, J.M. Coronado, Solar Energy on Demand: A Review on High Temperature Thermochemical Heat Storage Systems and Materials, Chem. Rev. 119 (2019) 4777–4816. doi:10.1021/acs.chemrev.8b00315.

[6] W. Lipiński, E. Abbasi-Shavazi, J. Chen, J. Coventry, M. Hangi, S. Iyer, A. Kumar, L. Li, S. Li, J. Pye, J.F. Torres, B. Wang, Y. Wang, V.M. Wheeler, Progress in heat transfer research for high-temperature solar thermal applications, Appl. Therm. Eng. 184 (2021) 116137. doi:10.1016/j.applthermaleng.2020.116137.

[7] F. Desai, J. Sunku Prasad, P. Muthukumar, M.M. Rahman, Thermochemical energy storage system for cooling and process heating applications: A review, Energy Convers. Manag. 229 (2021) 113617. doi:10.1016/j.enconman.2020.113617.

[8] C. Tregambi, M. Troiano, F. Montagnaro, R. Solimene, P. Salatino, Fluidized Beds for Concentrated Solar Thermal Technologies – A Review, Front. Energy Res. 9 (2021) 618421. doi:10.3389/fenrg.2021.618421.

[9] J.A. Almendros-Ibáñez, M. Fernández-Torrijos, M. Díaz-Heras, J.F. Belmonte, C. Sobrino, A review of solar thermal energy storage in beds of particles: Packed and fluidized beds, Sol. Energy. 192 (2019) 193–237. doi:10.1016/j.solener.2018.05.047.

[10] M.A. Rivero, D. Rodrigues, C.I.C. Pinheiro, J.P. Cardoso, L.F. Mendes, Solid – gas reactors driven by concentrated solar energy with potential application to calcium looping : A comparative review, Renew. Sustain. Energy Rev. 158 (2022) 112048. doi:10.1016/j.rser.2021.112048.

[11] C. Tregambi, P. Salatino, R. Solimene, F. Montagnaro, An experimental characterization of Calcium Looping integrated with concentrated solar power, Chem. Eng. J. 331 (2018)

833   794–802. doi:10.1016/j.cej.2017.08.068.

834 [12] R. Chirone, P. Salatino, P. Ammendola, R. Solimene, M. Magaldi, R. Sorrenti, G. De

835   Michele, F. Donatini, Development of a Novel Concept of Solar Receiver/Thermal

836   Energy Storage System Based on Compartmented Dense Gas Fluidized Beds, 14th Int.

837   Conf. Fluid. (2013).

838 [13] G. Flamant, G. Olalde, High temperature solar gas heating comparison between packed

839   and fluidized bed receivers-I, Sol. Energy. 31 (1983) 463–471. doi:10.1016/0038-

840   092X(83)90050-6.

841 [14] N. Gokon, T. Izawa, T. Kodama, Steam gasification of coal cokes by internally

842   circulating fluidized-bed reactor by concentrated Xe-light radiation for solar syngas

843   production, Energy. 79 (2015) 264–272. doi:10.1016/j.energy.2014.11.012.

844 [15] X. Li, L. Wei, C.W. Lim, J. Chen, P. Chu, W. Lipiński, N. Yan, Y. Dai, C.H. Wang,

845   Experimental and numerical study on thermal performance of an indirectly irradiated

846   solar reactor with a clapboard-type internally circulating fluidized bed, Appl. Energy.

847   305 (2022). doi:10.1016/j.apenergy.2021.117976.

848 [16] X. Li, J. Chen, Q. Hu, P. Chu, Y. Dai, C.H. Wang, Solar-driven gasification in an

849   indirectly-irradiated thermochemical reactor with a clapboard-type internally-circulating

850   fluidized   bed,   Energy   Convers.   Manag.   248   (2021)   114795.

851   doi:10.1016/j.enconman.2021.114795.

852 [17] M. Díaz-Heras, J.F. Belmonte, J.A. Almendros-Ibáñez, Experimental observations on

853   directly irradiated conical spouted and spout-fluid beds, Exp. Therm. Fluid Sci. 130

854   (2022) 110488. doi:10.1016/j.expthermflusci.2021.110488.

855 [18] M. Díaz-Heras, J.F. Belmonte, J.A. Almendros-Ibáñez, Experimental observations on

856   directly irradiated fluidized beds: Even and uneven fluidization, Exp. Therm. Fluid Sci.

857   120 (2021) 110242. doi:10.1016/j.expthermflusci.2020.110242.

858 [19] C. Tregambi, R. Chirone, F. Montagnaro, P. Salatino, R. Solimene, Heat transfer in

859   directly   irradiated   fluidized   beds,   Sol.   Energy.   129   (2016)   85–100.

860   doi:10.1016/j.solener.2016.01.057.

861 [20] S. Migliozzi, A. Paulillo, R. Chirone, P. Salatino, R. Solimene, Hydrodynamics of

862   compartmented fluidized bed for concentrated solar power and thermnal energy storage

863   applications, Fluid. XV. (2016). doi:10.1016/j.powtec.2016.12.052.

864 [21] T. Esence, E. Guillot, M. Tessonneaud, J.L. Sans, G. Flamant, Solar calcination at pilot

865   scale in a continuous flow multistage horizontal fluidized bed, Sol. Energy. 207 (2020)

866   367–378. doi:10.1016/j.solener.2020.06.098.

867   [22]   T. Esence, H. Benoit, D. Poncin, M. Tessonneaud, G. Flamant, A shallow cross-flow
868   fluidized-bed solar reactor for continuous calcination processes, Sol. Energy. 196 (2020)
869   389–398. doi:10.1016/j.solener.2019.12.029.

870   [23]   J. Gómez-Hernández, P.A. González-Gómez, J. V. Briongos, D. Santana, Technical
871   feasibility analysis of a linear particle solar receiver, Sol. Energy. 195 (2020) 102–113.
872   doi:10.1016/j.solener.2019.11.052.

873   [24]   C. Tregambi, C. Bevilacqua, M. Troiano, R. Solimene, P. Salatino, A novel autothermal
874   fluidized bed reactor for concentrated solar thermal applications, Chem. Eng. J. 398
875   (2020) 125702. doi:10.1016/j.cej.2020.125702.

876   [25]   S. Padula, C. Tregambi, R. Solimene, R. Chirone, M. Troiano, P. Salatino, A novel
877   fluidized bed "thermochemical battery" for energy storage in concentrated solar thermal
878   technologies, Energy Convers. Manag. 236 (2021) 113994.
879   doi:10.1016/j.enconman.2021.113994.

880   [26]   T. Uchino, C. Fushimi, Fluidized bed reactor for thermochemical heat storage using
881   Ca(OH)2/CaO to absorb the fluctuations of electric power supplied by variable
882   renewable energy sources: A dynamic model, Chem. Eng. J. 419 (2021) 129571.
883   doi:10.1016/j.cej.2021.129571.

884   [27]   C. Ortiz, J.M. Valverde, R. Chacartegui, L.A. Perez-Maqueda, P. Giménez, The
885   Calcium-Looping (CaCO3/CaO) process for thermochemical energy storage in
886   Concentrating Solar Power plants, Renew. Sustain. Energy Rev. 113 (2019) 109252.
887   doi:10.1016/j.rser.2019.109252.

888   [28]   E. Darwish, M. Mansouri, D. Yilmaz, H. Leion, Effect of Mn and Cu substitution on the
889   SrFeO3 perovskite for potential thermochemical energy storage applications, Processes.
890   9 (2021). doi:10.3390/pr9101817.

891   [29]   L. André, S. Abanades, Recent Advances in Thermochemical Energy Storage via Solid
892   – Gas Reversible Reactions at High Temperature, Energies. 13 (2020) 5859.
893   doi:doi:10.3390/en13225859.

894   [30]   SOCRATCES (SOlar Calcium-looping integRAtion for ThermoChemical Energy
895   Storage), https://socratces.eu/ . Last accessed: February 2022., (n.d.).

896   [31]   CALyPSOL (CALcium oxide LooPing through SOLar energy),
897   https://www.dlr.de/ff/en/desktopdefault.aspx/tabid-18130/28811_read-71705/ . Last
898   accessed: May 2022., (n.d.).

899   [32]   M.T. Dunstan, F. Donat, A.H. Bork, C.P. Grey, C.R. Müller, CO2 Capture at Medium
900   to High Temperature Using Solid Oxide-Based Sorbents: Fundamental Aspects,

901 Mechanistic Insights, and Recent Advances, Chem. Rev. 121 (2021) 12681–12745.
902 doi:10.1021/acs.chemrev.1c00100.

903 [33] A. Coppola, O. Senneca, F. Scala, F. Montagnaro, P. Salatino, Looping cycles for low
904 carbon technologies: A survey of recent research activities in Naples, Fuel. 268 (2020)
905 117371. doi:10.1016/j.fuel.2020.117371.

906 [34] C. Tregambi, P. Bareschino, D. Hanak, F. Montagnaro, F. Pepe, E. Mancusi, Modelling
907 of an integrated process for atmospheric carbon dioxide capture and methanation, J.
908 Clean. Prod. 356 (2022) 131827. doi:10.1016/j.jclepro.2022.131827.

909 [35] T. Shimizu, T. Hirama, H. Hosoda, K. Kitano, M. Inagaki, K. Tejima, A twin fluid-bed
910 reactor for removal of CO2 from combustion processes, Chem. Eng. Res. Des. 77 (1999)
911 62–68. doi:10.1205/026387699525882.

912 [36] S. Khosravi, S. Hossainpour, H. Farajollahi, N. Abolzadeh, Integration of a coal fired
913 power plant with calcium looping CO2 capture and concentrated solar power generation:
914 Energy, exergy and economic analysis, Energy. 240 (2022) 122466.
915 doi:10.1016/j.energy.2021.122466.

916 [37] J.P. Rincon Duarte, D. Kriechbaumer, B. Lachmann, S. Tescari, T. Fend, M. Roeb, C.
917 Sattler, Solar calcium looping cycle for CO2 capturing in a cement plant. Definition of
918 process parameters and reactors selection, Sol. Energy. 238 (2022) 189–202.
919 doi:10.1016/j.solener.2022.04.031.

920 [38] U. Tesio, E. Guelpa, V. Verda, Comparison of sCO2 and He Brayton cycles integration
921 in a Calcium-Looping for Concentrated Solar Power, Energy. 247 (2022) 123467.
922 doi:10.1016/j.energy.2022.123467.

923 [39] M. Benitez-Guerrero, B. Sarrion, A. Perejon, P.E. Sanchez-Jimenez, L.A. Perez-
924 Maqueda, J. Manuel Valverde, Large-scale high-temperature solar energy storage using
925 natural minerals, Sol. Energy Mater. Sol. Cells. 168 (2017) 14–21.
926 doi:10.1016/j.solmat.2017.04.013.

927 [40] M. Benitez-Guerrero, J.M. Valverde, P.E. Sanchez-Jimenez, A. Perejon, L.A. Perez-
928 Maqueda, Multicycle activity of natural CaCO3 minerals for thermochemical energy
929 storage in Concentrated Solar Power plants, Sol. Energy. 153 (2017) 188–199.
930 doi:10.1016/j.solener.2017.05.068.

931 [41] C. Tregambi, F. Di Lauro, F. Montagnaro, P. Salatino, R. Solimene, 110th Anniversary:
932 Calcium Looping Coupled with Concentrated Solar Power for Carbon Capture and
933 Thermochemical Energy Storage, Ind. Eng. Chem. Res. 58 (2019) 21262−21272.
934 doi:10.1021/acs.iecr.9b03083.

935 [42] Y. Yang, Y. Li, X. Yan, J. Zhao, C. Zhang, Development of thermochemical heat storage
936   based on CaO/CaCO3 cycles: A review, Energies. 14 (2021). doi:10.3390/en14206847.

937 [43] H. Guo, S. Wang, C. Li, Y. Zhao, Q. Sun, X. Ma, Incorporation of Zr into Calcium Oxide
938   for CO2 Capture by a Simple and Facile Sol-Gel Method, Ind. Eng. Chem. Res. 55
939   (2016) 7873–7879. doi:10.1021/acs.iecr.5b04112.

940 [44] K.T. Møller, T.D. Humphries, A. Berger, M. Paskevicius, C.E. Buckley,
941   Thermochemical energy storage system development utilising limestone, Chem. Eng. J.
942   Adv. 8 (2021) 100168. doi:10.1016/j.ceja.2021.100168.

943 [45] A.N. Antzara, A. Arregi, E. Heracleous, A.A. Lemonidou, In-depth evaluation of a ZrO2
944   promoted CaO-based CO2 sorbent in fluidized bed reactor tests, Chem. Eng. J. 333
945   (2018) 697–711. doi:10.1016/j.cej.2017.09.192.

946 [46] M. Benitez-Guerrero, J.M. Valverde, P.E. Sanchez-Jimenez, A. Perejon, L.A. Perez-
947   Maqueda, Calcium-Looping performance of mechanically modified Al2O3-CaO
948   composites for energy storage and CO2 capture, Chem. Eng. J. 334 (2018) 2343–2355.
949   doi:10.1016/j.cej.2017.11.183.

950 [47] A. Antzara, E. Heracleous, A.A. Lemonidou, Improving the stability of synthetic CaO-
951   based CO2 sorbents by structural promoters, Appl. Energy. 156 (2015) 331–343.
952   doi:10.1016/j.apenergy.2015.07.026.

953 [48] M. Heidari, M. Tahmasebpoor, A. Antzaras, A.A. Lemonidou, CO2 capture and fluidity
954   performance of CaO-based sorbents: Effect of Zr, Al and Ce additives in tri-, bi- and
955   mono-metallic configurations, Process Saf. Environ. Prot. 144 (2020) 349–365.
956   doi:10.1016/j.psep.2020.07.041.

957 [49] D. Choi, A.-H. Alissa Park, Y. Park, Effects of eutectic alkali chloride salts on the
958   carbonation reaction of CaO-based composites for potential application to a
959   thermochemical energy storage system, Chem. Eng. J. 437 (2022) 135481.
960   doi:10.1016/j.cej.2022.135481.

961 [50] M. Sayyah, Y. Lu, R.I. Masel, K.S. Suslick, Mechanical Activation of CaO-Based
962   Adsorbents for CO2 Capture, ChemSusChem. 6 (2013) 193–198.
963   doi:10.1002/cssc.201200454.

964 [51] M. Benitez-Guerrero, J.M. Valverde, A. Perejon, P.E. Sanchez-Jimenez, L.A. Perez-
965   Maqueda, Effect of milling mechanism on the CO2 capture performance of limestone in
966   the Calcium Looping process, Chem. Eng. J. 346 (2018) 549–556.
967   doi:10.1016/j.cej.2018.03.146.

968 [52] F. Di Lauro, C. Tregambi, F. Montagnaro, P. Salatino, R. Chirone, R. Solimene,

969 Improving the performance of calcium looping for solar thermochemical energy storage
970 and CO_2 capture, Fuel. 298 (2021) 120791. doi:10.1016/j.fuel.2021.120791.

971 [53] J.M. Valverde, M. Barea-López, A. Perejón, P.E. Sánchez-Jiménez, L.A. Pérez-
972 Maqueda, Effect of Thermal Pretreatment and Nanosilica Addition on Limestone
973 Performance at Calcium-Looping Conditions for Thermochemical Energy Storage of
974 Concentrated Solar Power, Energy and Fuels. 31 (2017) 4226–4236.
975 doi:10.1021/acs.energyfuels.6b03364.

976 [54] J. Arcenegui-Troya, P.E. Sánchez-Jiménez, A. Perejón, V. Moreno, J.M. Valverde, L.A.
977 Pérez-Maqueda, Kinetics and cyclability of limestone ($CaCO_3$) in presence of steam
978 during calcination in the CaL scheme for thermochemical energy storage, Chem. Eng. J.
979 417 (2021). doi:10.1016/j.cej.2021.129194.

980 [55] J. Arcenegui-Troya, P.E. Sánchez-Jiménez, A. Perejón, J.M. Valverde, L.A. Pérez-
981 Maqueda, Steam-enhanced calcium-looping performance of limestone for
982 thermochemical energy storage: The role of particle size, J. Energy Storage. 51 (2022).
983 doi:10.1016/j.est.2022.104305.

984 [56] A. Coppola, A. Esposito, F. Montagnaro, G. De Tommaso, F. Scala, P. Salatino, Effect
985 of exposure to SO_2 and H_2O during the carbonation stage of fluidised bed calcium
986 looping on the performance of sorbents of different nature, Chem. Eng. J. 377 (2019)
987 120626. doi:10.1016/j.cej.2018.12.086.

988 [57] L. Yang, G. Huang, Z. Huang, Optimized design of Ca-based thermochemical heat
989 storage materials for concentrated solar power, J. Energy Storage. 43 (2021) 103236.
990 doi:10.1016/j.est.2021.103236.

991 [58] H. Zheng, X. Liu, Y. Xuan, C. Song, D. Liu, Q. Zhu, Z. Zhu, K. Gao, Y. Li, Y. Ding,
992 Thermochemical heat storage performances of fluidized black $CaCO_3$ pellets under
993 direct concentrated solar irradiation, Renew. Energy. 178 (2021) 1353–1369.
994 doi:10.1016/j.renene.2021.07.026.

995 [59] Y. Da, Y. Xuan, L. Teng, K. Zhang, X. Liu, Y. Ding, Calcium-based composites for
996 direct solar-thermal conversion and thermochemical energy storage, Chem. Eng. J. 382
997 (2020) 122815. doi:10.1016/j.cej.2019.122815.

998 [60] A. Scaltsoyiannes, A. Antzaras, G. Koilaridis, A. Lemonidou, Towards a generalized
999 carbonation kinetic model for CaO-based materials using a modified random pore model,
1000 Chem. Eng. J. 407 (2021) 127207. doi:10.1016/j.cej.2020.127207.

1001 [61] G.M. Castilla, D.C. Guío-Pérez, S. Papadokonstantakis, F. Johnsson, D. Pallarès,
1002 Techno-economic assessment of calcium looping for thermochemical energy storage

1003   with CO2 capture, Energies. 14 (2021) 1–17. doi:10.3390/en14113211.

1004   [62]   B. Sarrion, J.M. Valverde, A. Perejon, L. Perez-Maqueda, P.E. Sanchez-Jimenez, On the

1005   Multicycle Activity of Natural Limestone/Dolomite for Thermochemical Energy Storage

1006   of   Concentrated   Solar   Power,   Energy   Technol.   4   (2016)   1013–1019.

1007   doi:10.1002/ente.201600068.

1008   [63]   B. Sarrión, A. Perejón, P.E. Sánchez-Jiménez, L.A. Pérez-Maqueda, J.M. Valverde, Role

1009   of calcium looping conditions on the performance of natural and synthetic Ca-based

1010   materials   for   energy   storage,   J.   CO2   Util.   28   (2018)   374–384.

1011   doi:10.1016/j.jcou.2018.10.018.

1012   [64]   S. Pascual, P. Lisbona, M. Bailera, L.M. Romeo, Design and operational performance

1013   maps of calcium looping thermochemical energy storage for concentrating solar power

1014   plants, Energy. 220 (2021) 119715. doi:10.1016/j.energy.2020.119715.

1015   [65]   S. Pascual, P. Lisbona, L.M. Romeo, Operation maps in calcium looping

1016   thermochemical energy storage for concentrating solar power plants, J. Energy Storage.

1017   55 (2022) 105771. doi:10.1016/j.est.2022.105771.

1018   [66]   C. Tregambi, P. Bareschino, E. Mancusi, F. Pepe, F. Montagnaro, R. Solimene, P.

1019   Salatino, Modelling of a concentrated solar power – photovoltaics hybrid plant for

1020   carbon dioxide capture and utilization via calcium looping and methanation, Energy

1021   Convers. Manag. 230 (2021) 113792. doi:10.1016/j.enconman.2020.113792.

1022   [67]   G.S. Grasa, J.C. Abanades, CO2 Capture Capacity of CaO in Long Series of

1023   Carbonation/Calcination Cycles, Ind. Eng. Chem. Res. 45 (2006) 8846–8851.

1024   doi:10.1021/ie0606946.

1025   [68]   G. Olivieri, A. Marzocchella, P. Salatino, A fluid-bed continuous classifier of

1026   polydisperse granular solids, J. Taiwan Inst. Chem. Eng. 40 (2009) 638–644.

1027   doi:10.1016/j.jtice.2009.05.011.

1028   [69]   G. Olivieri, A. Marzocchella, P. Salatino, Segregation of fluidized binary mixtures of

1029   granular solids, AIChE J. 50 (2004) 3095–3106. doi:10.1002/aic.10340.

1030   [70]   J.R. Grace, Fluidized-bed hydrodynamics, in: G. Hetsroni (Ed.), Handb. Multiph. Syst.,

1031   Washington: Hemisphere, 1982: pp. 8-1-8–64.

1032   [71]   C. Tregambi, R. Solimene, F. Montagnaro, P. Salatino, M. Marroccoli, N. Ibris, A.

1033   Telesca, Solar-driven production of lime for ordinary Portland cement formulation, Sol.

1034   Energy. 173 (2018) 759–768. doi:10.1016/j.solener.2018.08.018.

1035   [72]   S. Telschow, F. Frandsen, K. Theisen, K. Dam-Johansen, Cement formation-A success

1036   story in a black box: High temperature phase formation of portland cement clinker, Ind.

1037   Eng. Chem. Res. 51 (2012) 10983–11004. doi:10.1021/ie300674j.

1038   [73]   M. Alonso, Y. Álvarez Criado, J.R. Fernández, C. Abanades, CO2 Carrying Capacities
1039   of Cement Raw Meals in Calcium Looping Systems, Energy and Fuels. 31 (2017)
1040   13955–13962. doi:10.1021/acs.energyfuels.7b02586.

1041   [74]   M. Alonso, J.R. Fernández, J.C. Abanades, Kinetic Study of Belite Formation in Cement
1042   Raw Meals Used in the Calcium Looping CO2 Capture Process, Ind. Eng. Chem. Res.
1043   58 (2019) 5445–5454. doi:10.1021/acs.iecr.9b00813.

1044   [75]   J.M. Valverde, A. Perejon, L.A. Perez-Maqueda, Enhancement of fast CO2 capture by a
1045   nano-SiO2/CaO composite at Ca-looping conditions, Environ. Sci. Technol. 46 (2012)
1046   6401–6408. doi:10.1021/es3002426.

1047   [76]   R. Barker, The reversibility of the reaction CaCO3 $\rightleftarrows$ CaO+CO2, J. Appl. Chem.
1048   Biotechnol. 23 (1973) 733–742. doi:10.1002/jctb.5020231005.

1049   [77]   V. Moreno, J. Arcenegui-Troya, P. Enrique Sánchez-Jiménez, A. Perejón, R.
1050   Chacartegui, J. Manuel Valverde, L. Allan Pérez-Maqueda, Albero: An alternative
1051   natural material for solar energy storage by the calcium-looping process, Chem. Eng. J.
1052   440 (2022) 135707. doi:10.1016/j.cej.2022.135707.

1053